APPLIED SCIENCES AND ENGINEERING

# High-resolution fluorescence-guided transcranial ultrasound mapping in the live mouse brain

**Hector Estrada[1,2], Justine Robin[1,2]†, Ali Özbek[1,2], Zhenyue Chen[1,2], Anne Marowsky[1], Quanyu Zhou[1,2], Daniel Beck[1], Beau le Roy[1], Michael Arand[1], Shy Shoham[3]*, Daniel Razansky[1,2]***



**Understanding the physiological impact of transcranial ultrasound in rodent brains may offer an important preclinical model for human scale magnetic resonance–guided focused ultrasound methods. However, precision tools for high-resolution transcranial ultrasound targeting and real-time in vivo tracking of its effects at the mouse brain scale are currently lacking. We report a versatile bidirectional hybrid fluorescence-ultrasound (FLUS) system incorporating a 0.35-mm precision spherical-phased array ultrasound emission with a fiberscope-based wide-field fluorescence imaging. We show how the marriage between cortex-wide functional imaging and targeted ultrasound delivery can be used to transcranially map previously undocumented localized fluorescence events caused by reversible thermal processes and perform high-speed large-scale recording of neural activity induced by focused ultrasound. FLUS thus naturally harnesses the extensive toolbox of fluorescent tags and ultrasound's localized bioeffects toward visualizing and causally perturbing a plethora of normal and pathophysiological processes in the living murine brain.**

## INTRODUCTION

Transcranial ultrasound of both high and low intensities is increasingly used to treat and study the brain with high spatial and temporal specificity (*1*). Several methods have been developed in the context of magnetic resonance–guided focused ultrasound (MRgFUS) therapy to characterize the effects of high ultrasonic intensity in brain tissue (*2*) and monitor the occurrence of thermal lesions (*3*). The therapy's success depends on delivering ultrasound power sufficient for reaching the coagulation threshold while concurrent monitoring is achieved with MR thermometry (*1*). Similar efforts have been made to study the subtle effects of low intensity ultrasound, for example, on brain function (*4*), on blood-brain barrier opening (*5*), and on a variety of additional physiological mechanisms and targets (*6*).

Murine models play a central role across biomedical preclinical and basic research and are likely to play a similar role in unraveling the various effects of applying FUS of different regimes to the brain, particularly, when considering the multiple confounds present during in vitro experiments (*7*, *8*). Multiple methods have been deployed, e.g., to examine mouse brain responses to an ultrasonic stimulus including electrode recordings (*8*), muscle electromyography (*9*), laser speckle (*10*), optical intrinsic signal (*11*), and wide-field fluorescence imaging (*12*, *13*). However, these studies used unfocused or weakly focused beams measuring multiple millimeters across, which target very large cortical, subcortical, and peripheral sections of the mouse central nervous system, thus not faithfully resembling the human MRgFUS case (*1*, *14*). Moreover, when the ultrasound wavelength is not scaled down to generate a tightly focused spot inside the mouse head, some undesired ultrasound field patterns may further occur, such as standing waves in the mouse cranium (*15*). The spatial specificity has been improved using higher ultrasound frequencies (*16*), but no concurrent functional readout was available to monitor neural activities in the mouse brain.

Another major advantage of murine models is the availability of a powerful toolbox of fluorescent indicators for monitoring brain physiological processes in vivo, including indicators for observing brain activity and a host of other (patho-)physiological processes like glymphatic clearance, stroke, and immune cell trafficking, all the way from the cellular scale to the entire mouse cortex (*17*–*22*). This toolbox opens up intriguing possibilities for integrated multimodal studies to examine dynamic properties of tissue response to FUS. However, the efficient combination between precise transcranial FUS delivery and functional neuroimaging has so far been limited to low-resolution regimes and/or limited field of view (FOV) (*12*, *13*). Here, we fill this gap by introducing a versatile bidirectional hybrid fluorescence ultrasound (FLUS) system incorporating a high-precision FUS delivery by means of a spherical phased array with a fiberscope-based cortex-wide fluorescence imaging. To achieve accurate (submillimeter) in situ targeting despite strong skull-induced aberrations, we further introduce a fluorescence-based analog of MRgFUS harnessing the dependence of fluorescent protein brightness on temperature (*23*). This resulted in rapid negative fluorescence changes in the ultrasound focal zone in vivo, an effect that can reliably be represented by a thermal model. We use the new system to observe cortex-wide dynamics of spreading depolarization waves in the mouse brain triggered by high-intensity FUS exposures. FLUS may thus aid to exploit the full potential of murine models in studies of the modulation of normal and pathological brain physiology by targeted FUS, further providing an effective tool for investigating safe stimulation regimes and undesired side effects of the ultrasound delivery.

## RESULTS

### Characterization of transcranial FUS delivery

Simultaneous FUS and wide-field fluorescence imaging (Fig. 1A) is accomplished by combining a wide-angle 512-element spherical ultrasound array with a fiberscopic insert (*24*) consisting of 100,000 single

[1]Institute of Pharmacology and Toxicology, University of Zurich, Switzerland. [2]Institute for Biomedical Engineering, Department of Information Technology and Electrical Engineering, ETH Zurich and University of Zurich, Zurich, Switzerland. [3]Department of Ophthalmology and Tech4Health and Neuroscience Institutes, NYU Langone Health, New York, NY 10016, USA.
*Corresponding author. Email: daniel.razansky@uzh.ch (D.R.); shoham@nyu.edu (S.S.)
†Present address: Institut Langevin, ESPCI Paris, PSL University, CNRS, 75005 Paris, France.

mode fibers for delivering the excitation light and collecting fluorescence emission (see Materials and Methods). The ultrasound focus can be flexibly steered across an effective range of 6 mm in all three dimensions (*25*), while the entire mouse cortex (12-mm FOV) can be simultaneously imaged in the fluorescence mode (Fig. 1B). We first characterized how the transcranial FUS delivery is affected by the mouse skull (Fig. 1C). For this, the ultrasound intensity in the focal region was measured by a calibrated 75-μm-diameter hydrophone (Precision Acoustics, UK) with and without the presence of an excised mouse skull sample. At 3 MHz, the skull insertion loss reaches 6 dB, thus effectively reducing the free field pressure at the focus by 50% when operating transcranially. The focal spot is shifted by less than 100 μm, and its size increases by 11% because of the skull-induced distortions (Fig. 1D and E), effects that have previously been reported for human MRgFUS (*14*). In agreement with previous results, the full width at half maximum of the focal region remains below 400 μm (Fig. 1E) (*25*), thus providing an unmatched spatial specificity for studying the FUS effects in vivo.

## Targeted transcranial FUS induces a focal fluorescence response

Robust generation of focal fluorescence dips was observed in response to continuous (150-ms duration) transcranial sonication of cortical locations in GCaMP6f-expressing mice (Fig. 2A) under ketamine-xylazine anesthesia. The dips were highly localized in time (Fig. 2, B and F) and space (Fig. 2, D and E) around the ultrasound focal points for an estimated transcranial pressure of 3 MPa. The background resting state calcium oscillations due to the brain activity under anesthesia (Fig. 2B) make the detection of single fluorescence dips difficult. However, resting state cancelation (RSC) can improve the signal-to-noise ratio (SNR) owing to the high degree of interhemisphere correlation (Fig. 2C). The different locations were targeted sequentially (Fig. 2F) using the precise three-dimensional beam-forming capabilities of the spherical ultrasound array. The two spots do not manifest the same fluorescence dip intensity, presumably due to the skull's curvature and inhomogeneities. This constitutes a well-known limitation of transcranial FUS delivery, now made evident by simultaneous fluorescence imaging. We then used green fluorescent protein (GFP)–expressing bacteria to validate the appearance of focal fluorescence dip in controlled in vitro environment and better understand the origin and characteristics of this effect (fig. S1). GCaMP-family indicators are constructed from circularly permuted GFPs, so this fairly simple experiment was designed to test for induced responses outside the context of neuronal calcium dynamics. We observed similar fluorescence dips, which also displayed transient phenomena with similar relaxation times (Fig. 2, G to H). This suggests a FUS-triggered thermal process unrelated to calcium dynamics. GFP exhibits negative dependence of fluorescence brightness on temperature, following an approximately −0.9%/°C slope (*23*). The negative fluorescence change $\Delta F_{US}$ also increases with the ultrasound intensity (Fig. 2I).

## FUS-induced fluorescence response is accurately predicted by a thermal model

In vitro measurements in mouse brain slices expressing GCaMP6f (Fig. 3A) unveiled a stronger temperature dependence of fluorescence with a slope of −1.9 ± 0.7%/°C. In these experiments, the temperature was controlled using a water bath while a thermocouple monitored the brain slice's temperature and the camera recorded changes in fluorescence. We next set out to establish whether the temporal shape of the fluorescence dips observed in vivo could be ascribed to the underlying temperature transients induced by the relatively high ultrasound pressure (3 MPa). To assess how ultrasound induces thermal effects, one may rely on the basic relation (*26*) linking the temperature increase $\Delta T_{max}$ (°C) to the volumetric rate of heat generation $Q$ (W/cm$^3$) and exposure duration $\Delta t$ (s) via

$$\Delta T_{max} = Q \cdot \Delta t / C_v = 2\alpha \cdot I_{TA} \cdot \Delta t / C_v \quad (1)$$

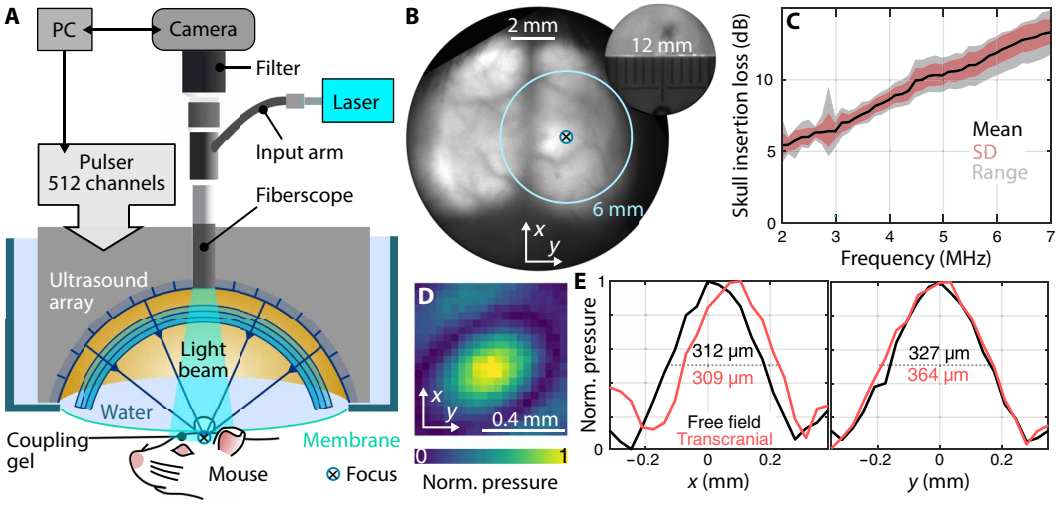


**Fig. 1. Experimental setup and characterization.** (**A**) Schematic of the integrated wide-field fluorescence imaging and high-precision transcranial ultrasound system FLUS. (**B**) Fluorescence image of a mouse brain expressing GCaMP6f through the intact scalp and skull. A crosshair indicates the position of the array's focus and the 6-mm circle the extent of the three-dimensional focus- steering range. The inset shows the extent of the field of view. (**C**) Skull insertion loss [mean, standard deviation (SD), and range] as a function of frequency measured using a hydrophone. (**D**) Normalized ultrasound pressure measured transcranially at 3 MHz. (**E**) Focal spot size at 3 MHz in free field (without the skull) and with the mouse skull in the ultrasound propagation path.

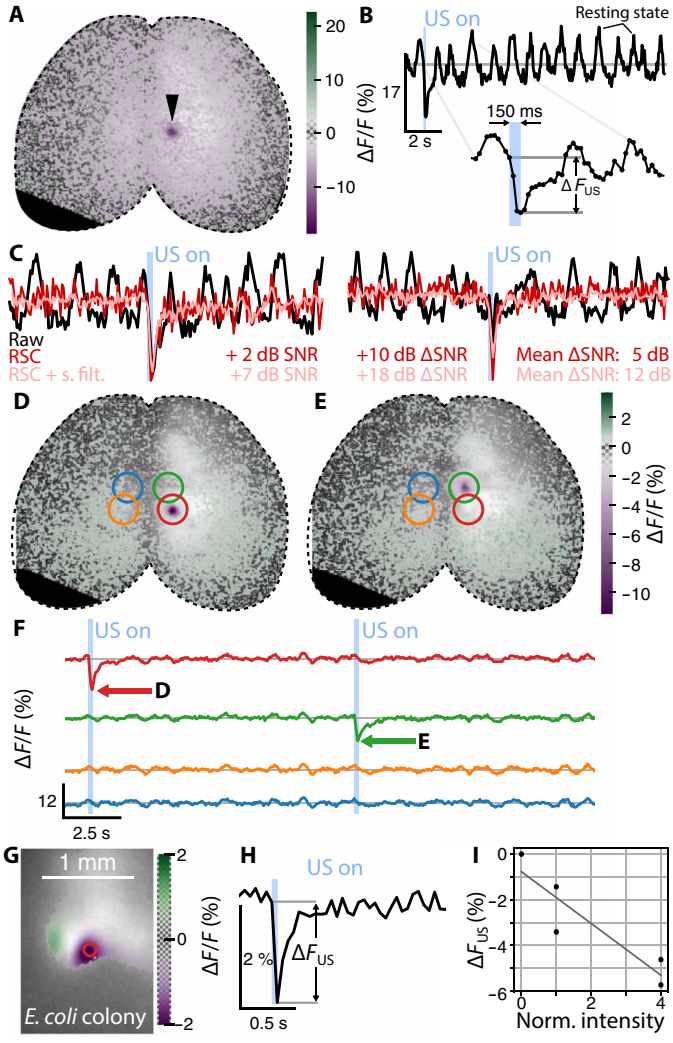


**Fig. 2. Wide-field recording of a mouse brain expressing GCaMP6f during sequential FUS delivery.** (**A**) Relative fluorescence change overlaid on the baseline fluorescence image shown on a gray scale. The arrowhead indicates the point of ultrasound delivery at the instant of minimum fluorescence. (**B**) Time trace of the relative change in fluorescence at the center of the ultrasound delivery region shown in (A). Details on the ultrasound delivery time shown on the inset. (**C**) RSC on two single FUS sonication. Addition of moderate spatial filtering (2 pixels wide) further improves the SNR. (**D** and **E**) Relative fluorescence change during ultrasound delivery at the targeted regions (red and green rings) averaged over 24 stimulation cycles. (**F**) Fluorescence time traces from (D) and (E) showing the average response of a single pixel at the ring's center. (**G**) Averaged relative fluorescence change observed in *E. coli* colonies at the instant of minimum fluorescence overlaid on average fluorescence in gray scale. (**H**) Relative fluorescence change at the position of the red circle from (G). The emission was repeated for five cycles with a period of 2 s. (**I**) Relative fluorescence change as a function of the normalized ultrasound intensity.

where α is the ultrasonic frequency–dependent absorption coefficient (Table 1), $I_{TA}$ denotes the time-averaged ultrasonic intensity, and $C_v$ (J/°C) is the medium's heat capacity per unit volume. As intensity is proportional to the square of acoustic pressure, one may derive the temperature increase in the brain for different peak pressures and frequencies using the thermal diffusion model (*27*) considering measured or known ultrasound tissue properties (*27*, *28*).

When linking the FUS-mediated temperature increase with the temperature dependence of GCaMP fluorescence (Fig. 3A), a sharp linear decrease of fluorescence intensity is expected, followed by a slower recovery as the heat diffuses out from the ultrasonic focus into the surrounding tissue. By averaging 24 sequential emission cycles, a clearer account of the thermal process can be observed by means of concurrent epifluorescence measurements (Fig. 2F). In particular, a sharp linear fluorescence decay occurs during the sonication followed by a slower recovery to baseline. Moreover, expanding the averaged in vivo dataset to include 140 emission cycles (seven mice and nine stimulation spots) and using RSC results in a clear representation of the spatio-temporal footprint of the thermal process (Fig. 3, B to D) closely resembling predictions made by the bioheat model (*29*) for the given brain tissue parameters and acoustic intensity at the focus. We calculate $\Delta T_{max}$ = 3.6°C (Eq. 1) for the given emission parameters (3 MHz, 150 ms, 3 MPa, sequence 1; Table 1), which can be translated to a relative −6.9% change in fluorescence when considering the measured GCaMP6f temperature dependence, thus closely resembling the experimentally observed ~7% fluorescence dip at the ultrasound focal spot (Fig. 3). Extending the comparison to nearby regions (Fig. 3B), one can further observe a good agreement between the thermal model and experimental data both in space and time (Fig. 3E). The spot size of 287 μm (Fig. 3D) is smaller than the transcranially measured spot (Fig. 1, D and E) because ultrasound heating is governed by the acoustic intensity, which, in turn, depends on the pressure squared.

## Functional consequences of precise FUS delivery

We next applied functional connectivity analysis to the cortex-wide calcium imaging data (*30*) to explore whether FUS delivery induces network level changes in the brain (Fig. 4). Seven regions on each hemisphere (Fig. 4A), chosen from the Allen Mouse Brain Atlas (*31*), were correlated against each other using a seed in datasets acquired before (Fig. 4B) and after (Fig. 4C) 20 pulsed sonications (3 MPa, 150-ms duration) to the left hemisphere of $n$ = 3 mice under 1.2% isoflurane anesthesia. It was determined that the connectivity matrices after sonication closely resemble the baseline measurements both qualitatively (Fig. 4, D and E) and statistically ($P > 0.05$ across all comparison, paired $t$ test; fig. S5). This lack of functional effect was further corroborated by negative histological findings (Fig. 4G) in stainings for cell nuclei [4′,6-diamidino-2-phenylindole (DAPI)] and apoptosis [TUNEL (terminal deoxynucleotidyl transferase–mediated deoxyuridine triphosphate nick end labeling) and Fluoro-Jade C] and summarized in fig. S2.

In contrast, when delivering a more intense (3.9 MPa) yet shorter (100 ms) sonications into $n$ = 3 mice under 1.2% isoflurane anesthesia, we identified negative functional connectivity changes of up to 2 σ across a substantial part of the brain network affecting mostly the primary somatosensory (SSp) cortex (Fig. 4H). Upon correction for multiple testing (green color scale), we found an interhemispheric connectivity decrease between SSpbfd-R and MOp-L, RSP-L ($P < 0.05$). Consistently, histological stainings revealed enhanced immunoglobulin G (IgG) immunolabeling around a pial vessel at the focal site, suggesting compromised blood-brain barrier ($n$ = 4 mice; Fig. 4I); (perivascular) microglia and astrocytic gliosis provided further evidence for the blood-brain barrier disruption and local inflammation triggered by the FUS stimulus (figs. S3 and S4). These complementary pieces of evidence suggest that intense FUS-triggered phenomena can induce plastic cellular- and network-level

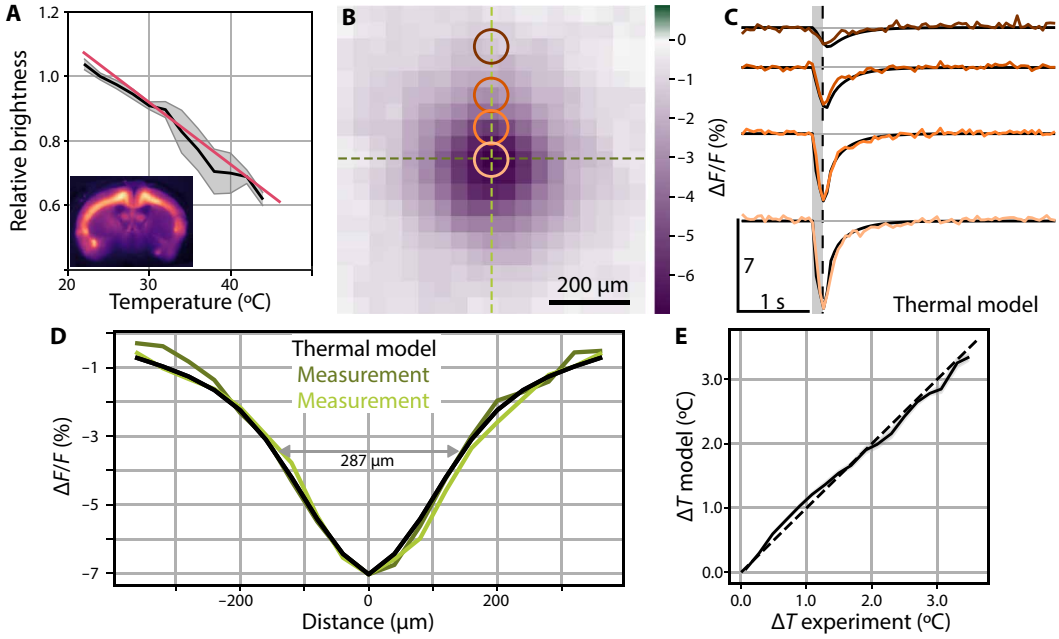


**Fig. 3. Average fluorescence dip characterization with a thermal model.** (**A**) Change in fluorescence as a function of the temperature in a brain slice expressing GCaMP6f. An affine fit to four brain slices yields a fluorescence change of −1.9 ± 0.7%/°C. (**B**) Average fluorescence dip ($n = 7$, 140 stimulation cycles) at the instant of the minimum fluorescence. (**C**) Time traces of the average dip compared with the thermal model from the bioheat equation labeled following the rings on (B). The gray region depicts the instant of the FUS delivery, while a dashed vertical line indicates the time instant shown in (B). (**D**) Characterization of the spatial extent of the fluorescence dip compared against the thermal model. Dark and light green experimental curves correspond to cross sections of the same colors in (B). (**E**) Inferred relative temperature change for the model and the measured data. Gray region depicts the SEM, whereas the dashed line shows the identity map.

**Table 1. Acoustic parameters for ultrasound emissions and CSD occurrence.** The pressure was measured using a hydrophone through an excised mouse skull. Thermal constants used to calculate the temperature increase and the ultrasound properties were adopted from (*27*). An ultrasound absorption of 16 Np/m was used for the mouse brain, within the upper bound of 21 Np/m extrapolated from the measured attenuation from a mouse brain slice using acoustic microscopy. Some mice were sonicated with more than one sequence.

| | Pulse duration (ms) | Pressure (MPa) | $I_{SPPA}$ (W/cm$^2$) | $\Delta T_{max}$ (°C) | Times delivered | Number of mice | CSD | CSD probability (%) |
|---|---|---|---|---|---|---|---|---|
| 1 | 150 | 3 | 284 | 3.6 | 250 | 12 | 0 | 0 |
| 2 | 100–300 | 3–3.9 | 284–479 | 4.1–7.3 | 23 | 10 | 2 | 8.7 |
| 3 | 150 | 4.8 | 724 | 9.3 | 5 | 3 | 5 | 100 |

effects, prompting a further exploration of network-wide events triggered by increasingly intense sonication pulses.

## Mesoscopic fluorescence imaging reveals dynamics of FUS-induced cortical spreading depression

A potential key advantage of our system is the ability to precisely monitor both the focal physical tissue perturbations and dynamics of their physiological impact at the whole-cortex level. When increasing the stimulation time to 300 ms under isoflurane anesthesia, we observed the initiation and propagation of a cortical spreading depression (CSD) in the right hemisphere (Fig. 5, A to E). The wave originates at the FUS delivery point (Fig. 5A) but remains unnoticed until 16 s after stimulation. The dip induced by the next stimulus occurring 30 s after the first one is visible in the time trace (Fig. 5E). After 44.45 s, the wave reaches a maximum 165% fluorescence increase from the baseline at the FUS delivery location (Fig. 5B), although the global maximum of the signal increase exceeds 200%. The CSD continues propagating across the right hemisphere (Fig. 5C), further inducing negative fluorescence changes down to −40% (Fig. 5D). CSDs were also triggered by higher pressures (see Fig. 5F and Table 1). Stimulation sequence 2 only triggered two CSD events over 23 sonications (10 mice), whereas sequence 3 resulted in a robust CSD for each sonication (five CSD events in three mice). In all the observed cases, the CSDs are confined to one hemisphere but manifest slightly different propagation dynamics depending on pressure (Fig. 5, G to I). Ex vivo histological analysis revealed high c-FOS immunoreactivity across the entire cortex affected by the CSD (fig. S6). The delay between the FUS emission and CSD's onset appears to be dependent on the pressure [or spatial peak pulse averaged intensity ($I_{SPPA}$)] with shorter delays observed for higher pressure levels (Fig. 5I). However, the propagation speed does not follow the same trend. Considering the time required for fluorescence to peak at locations 3 mm away from the FUS delivery point (Fig. 5J), the highest pressure (4.9 MPa) resulted in the slowest wave propagation

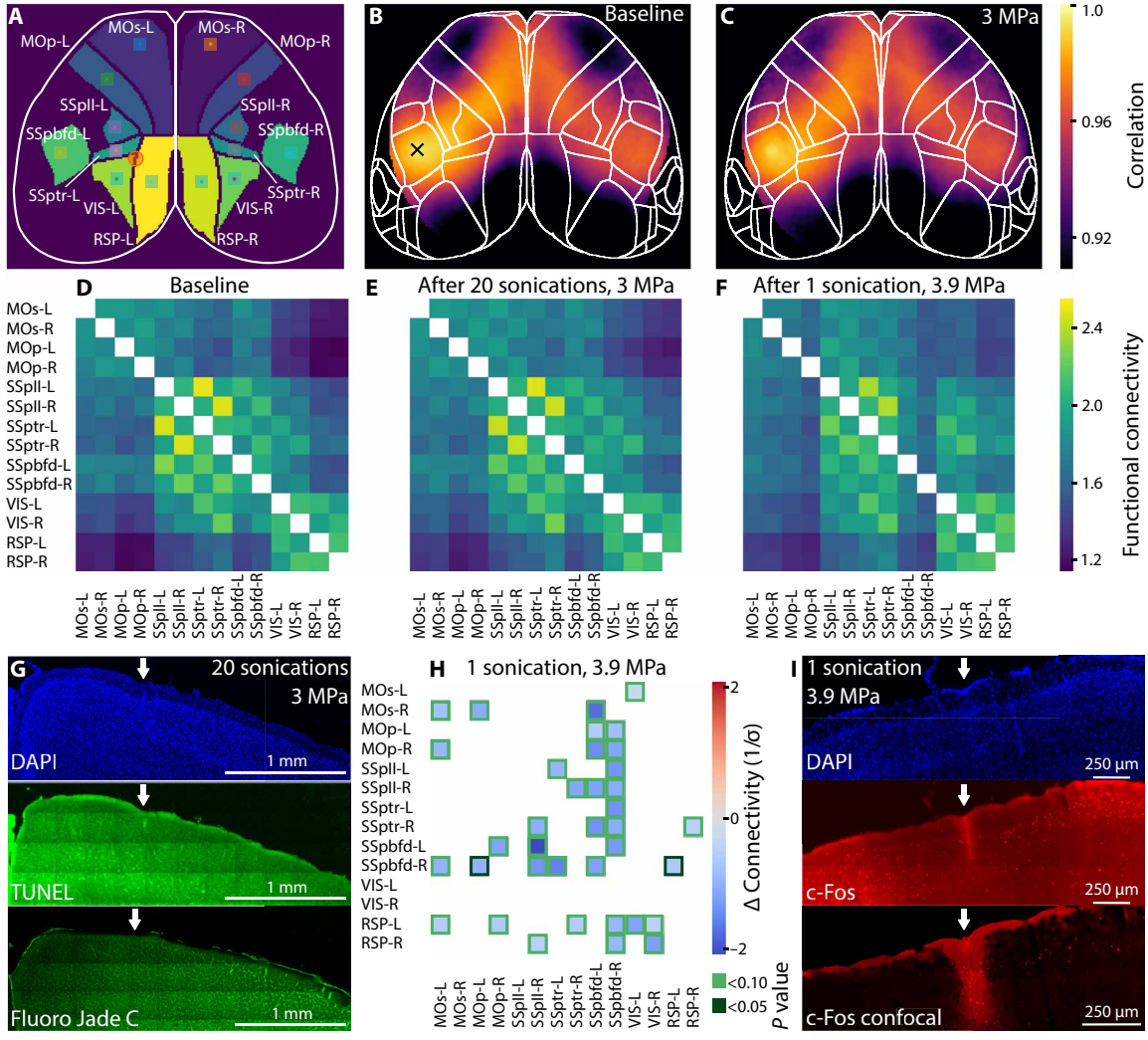


**Fig. 4. Functional connectivity (FC) before and after FUS delivery.** (**A**) Mouse brain schematic showing the regions included in the FC. Squares represent the seeds (7 × 7 pixels) while the orange circle depicts the FUS delivery spot. Average Pearson's correlation ($n = 3$) map calculated before (**B**) and after 20 sonications using sequence 1 (**C**). The cross (B) shows the seed position whereas the orange circle encloses the FUS delivery point. The Fisher *z*-transformed FC is shown in (**D** to **F**) for the baseline, 20 FUS emissions at 3 MPa (three mice) (E) and 1 emission at 3.9 MPa (three mice). (**G**) Coronal mouse brain slice at the point of FUS delivery stained with DAPI, TUNEL assay, and Fluoro-Jade C. Sonications for a more conclusive histological analysis were performed on the right hemisphere (see Materials and Methods). (**H**) Difference after FUS delivery in standard units (*z* score) and masked for multiple-testing corrected $P < 0.1$ from a paired *t* test. Dark-green squares show $P < 0.05$. (**I**) Histology analysis on coronal slices after single sonication at 3.9 MPa stained with DAPI and c-Fos imaged with wide-field and confocal microscopy.

speed of 3.9 mm/min. The fastest speed of 6.1 mm/min was attained for 3.9 MPa and the shortest emission time of 100 ms. The measured CSD propagation speeds are generally in agreement with previous observations ranging from 1 to 8 mm/min (*32*), but faster than the 2.5 mm/min reported for focal ischemia (*19*).

## DISCUSSION

We report on the first implementation of bidirectional hybrid FLUS system incorporating a high-frequency spherical-phased array for high-precision sonication and a fiberscope-based system for wide-field fluorescence imaging of the whole murine cortex. The system was capable of observing, fully noninvasively, previously undocumented effects of medium-intensity FUS delivery into the mouse brain. Fluorescence imaging revealed well-defined dips, confined in time and space to the FUS delivery points, arguably produced by a local temperature increase, which is unrelated to neuronal activity. This was further confirmed by observing the same dips also in GFP-loaded bacteria (Fig. 2G). The decrease of fluorescence brightness with temperature can be attributed to dynamic quenching (*33*). This well-known effect is related to absorption of the excited state's energy of the fluorophore via collisions with surrounding molecules, which does not lead to fluorescence emission. The dips were accurately predicted by a thermal model taking into account the GCaMP6f fluorescence brightness dependence on temperature. The latter was assessed without applying ultrasound by directly measuring temperature in a mouse brain slice (Fig. 3A). No signs of brain damage were found for 3-MPa focal pressures (sequence 1).

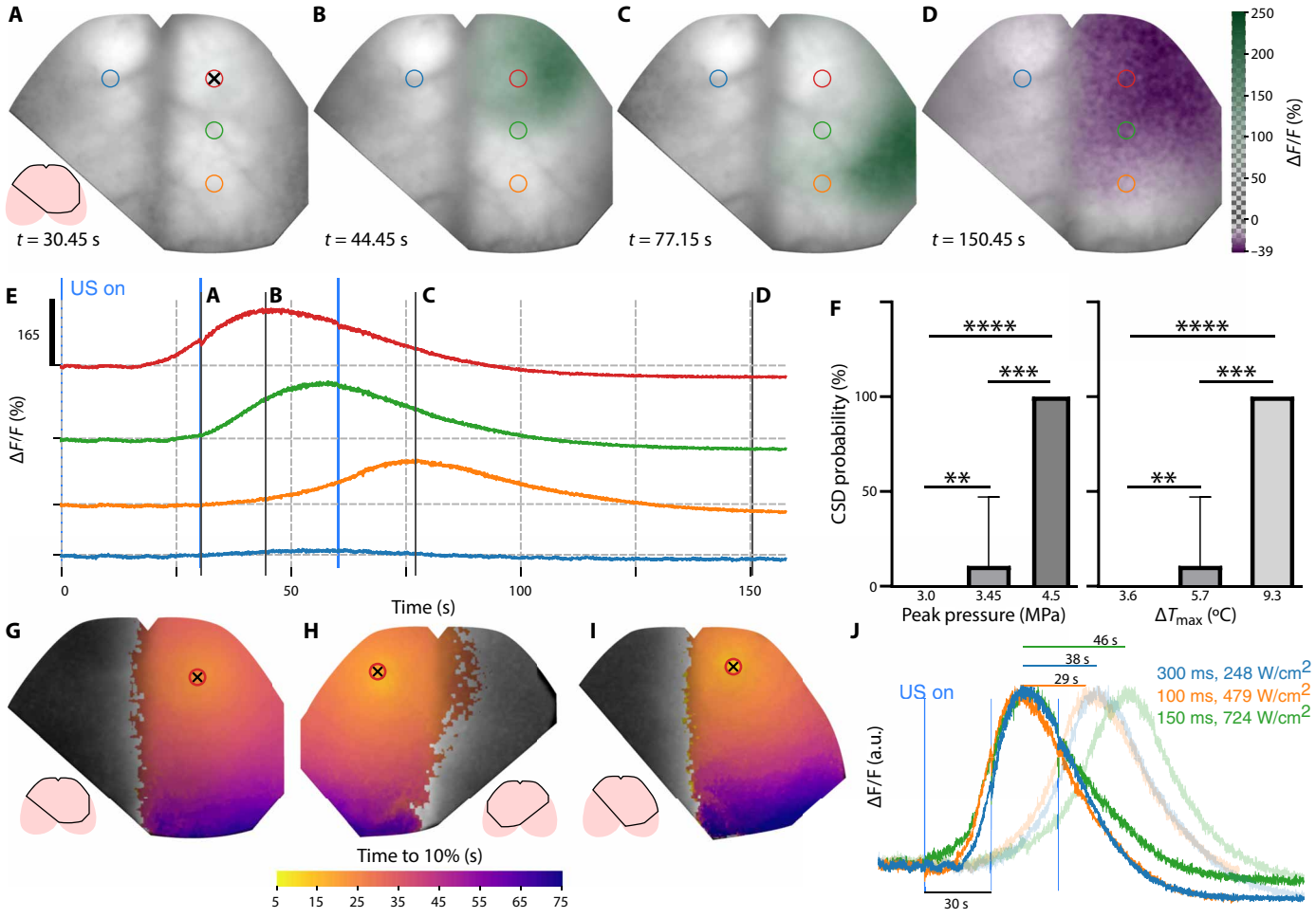


**Fig. 5. Wide-field recording of a CSD triggered by focused noninvasive ultrasound delivery.** (**A** to **D**) Relative fluorescence changes at different time points overlaid on baseline fluorescence shown in gray scale. (**E**) Time traces of the relative change in fluorescence at the points labeled by rings in (A). Ultrasound delivery point indicated by a crosshair. Light blue vertical lines at $t = 0$, 30, and 60 s. Represents the onset of consecutive ultrasound emission. Solid black vertical lines indicate the instants of the wide-field images shown in (A) to (D). (**F**) Mean probability of triggering a CSD as a function of the peak pressure and maximum temperature change. SD depicted by whiskers and the Mann-Whitney test. $^{**}P < 0.01$, $^{***}P \leq 0.001$, and $^{****}P \leq 0.0001$. (**G** to **I**) Maximum intensity projection of the relative fluorescence change color-coded for time to 10% of the peak values for stimulation sequences 2 (G), 2 (H), and 3 (I). (**J**) Normalized fluorescence change with the colors represented by labels indicating the pulse duration and the $I_{SPPA}$. Lines above the main peak show the time delay 3 mm away from the stimulated spot (transparent curves).

Upon longer sonication (e.g., 300 ms), cortical spreading depolarization events were triggered and observed in real time with FLUS as they propagated across the cortex.

The developed system, together with our findings on thermal dependence of fluorescence may provide a convenient alternative to MR imaging (MRI) thermometry for monitoring transcranial FUS experiments in mice. Note that for our experimental paradigm, the entire thermal process occurred within the time needed to acquire a single MRI thermometry frame (*2*, *3*). Future work should provide a reliable and quantitative model for fluorescence temperature dependence, accounting for the subjacent calcium dynamics.

Furthermore, one of the major challenges hindering the understanding of physical mechanisms underlying the action of low- and medium-intensity ultrasound on the brain is the lack of direct visualization of the large-scale brain activity and thermal effects concurrent with the sonication (*4*). Our results could fill this gap, with the advantage that fluorescence imaging offers a large versatility of neural activity indicators (*17*, *18*), to study all aspects of brain response.

Moreover, applying FLUS to the study of FUS effects on head-restrained awake animals could provide valuable insights overcoming the limitations of systems lacking precise focusing, three-dimensional beam steering, and cortex-wide imaging capabilities. Data processing tools for motion correction and single fluoro-thermal tag detection should be developed for experiments in awake animals.

The direct induction and observation of CSD opens new possibilities to study FUS-induced brain activity and its role in multiple neurological disorders, such as stroke and traumatic brain injury (*32*). Note that the alternative CSD triggering techniques, such as intracranial injection or topical application of KCl to the exposed cortex (*34*), optogenetic excitation (*35*), electrical stimulation (*36*), and embolic middle cerebral artery occlusion (*19*), all require invasive and complicated surgical procedures completely avoided with FLUS. This benefit would be particularly relevant to inducing and

monitoring CSD and its effects throughout longitudinal studies without the need for surgery or craniotomy. The negative fluorescence change observed after the CSD is deemed to agree with the entrance of CSF to the perivascular space (*19*). FUS has previously been demonstrated to trigger CSD because of temperature increase, with a threshold temperature of 47°C (*37*). This might explain the robust CSD triggering with sequence 3 for which the focal temperature reached ~46°C. On the other hand, delivering 3.9-MPa focal pressures over 100 ms only increases the temperature by 4.1°C, indicating that the respective CSD triggering mechanism is dominated by radiation force inducing blood-brain barrier disruption, as also confirmed by histology (Fig. 4I). The vascular disruption was still detectable at the network level using functional connectivity analysis (Fig. 4), although it was not responsible for triggering the CSD, further underscoring the versatility of FLUS to monitor FUS effects in vivo.

The present study was focused on relatively high ultrasound pressures between 3 and 5 MPa, i.e., $I_{SPPA}$ in the 280 to 730 W/cm$^2$ range. In contrast to MRI, the time resolution of fluorescence imaging is determined by the fluorescence lifetime in the nanosecond range (*38*). Thus, FLUS opens the possibility for fast fluorescence imaging of physical effects of short ultrasound pulses, used, e.g., to guide light through scattering medium (*39*) or monitor shock wave therapy (*40*), while monitoring their effect on the much slower neural responses through calcium imaging. In addition, lower pressures could also be investigated to study more subtle neuromodulatory effects, so far not directly observed using wide-field fluorescence (*12*, *13*). In this scenario, the FLUS system would be particularly useful not only for monitoring the neuronal responses but also for assessing or mitigating any adverse effects, such as irreversible changes of fluorescence due to temperature or CSD.

In summary, FLUS naturally harnesses the extensive toolbox of fluorescent tags and FUS-localized biological effects toward visualizing and causally perturbing a plethora of normal and pathophysiological processes in the living murine brain. It further allows the simultaneous observation and discernment between thermally and ultrasonically induced tissue responses in the same experiment. FLUS thus offers a valuable platform for observing ultrasound-evoked cerebral response and testing the general safety of transcranial FUS methods in small animal models.

## MATERIALS AND METHODS

### Integrated wide-field fluorescence imaging and ultrasound delivery (FLUS) system

The FUS delivery subsystem consists of a wide-angle spherical ultrasound array (Imasonic, France) featuring 512 transducer elements driven by a custom-designed multichannel electronics with a maximum digital temporal resolution of 5.5 ns (Falkenstein Mikrosysteme GmbH, Germany). The array was immersed in deionized water and coupled to the sample using a thin plastic membrane that is transparent to both light and ultrasound (Fig. 1A). A personal computer (PC) controlled the FUS emission by means of a graphical user interface implemented in MATLAB (2020, MathWorks Inc., Natick, USA).

Fluorescence imaging was performed simultaneously with the FUS emission through an 8-mm-diameter hole in the ultrasound array (Fig. 1A). For this, a custom-made fiberscope was used comprising 100,000 individual single-mode fibers (Zibra Corporation, Westport, MA, USA). The fiberscope covers an effective 12-mm-diameter circular FOV at 44-µm lateral resolution (Fig. 1B). Its input arm is coupled to the laser source, while the imaging arm is connected to an electron-multiplying charge-coupled device camera (iXon Life, Andor, UK) operated at 20 frames/s. A band-pass filter (MF525-39, Thorlabs, Newton, NJ, USA) blocked the excitation light (Sapphire LPX, continuous wave of 488 nm, Coherent Europe, Utrecht, The Netherlands) at the camera input, thus enabling fluorescence imaging. The PC controls the FUS emission while it also collects the camera images via the Andor Solis software interface.

### Image-guided positioning of the focal ultrasound spot

Because of the small size of the ultrasound focal spot, it is crucial to accurately map its location in three dimensions. We therefore used volumetric optoacoustic tomography (VOT) with the same spherical array to adjust the relative position between the ultrasound array and the sample. VOT imaging was performed with a separate digital sampling interface, as previously described (*25*). Since no concurrent FUS transmission and VOT recordings were possible, mapping of the ultrasound array and the sample position was performed before each FUS delivery experiment. The excitation light delivery for VOT imaging is accomplished by guiding pulses (~10 ns, 10 mJ at 488 nm) from an optical parametric oscillator laser (SpitLight; InnoLas Laser GmbH, Krailling, Germany) through a separate illumination bundle integrated into the fiberscopic arm (*24*).

### In vivo mouse experiments

All procedures involving mice conformed to the national guidelines of the Swiss Federal Act on animal protection and were approved by the Cantonal Veterinary Office Zurich (ZH161/18). Animals were housed in individually ventilated cages inside a temperature-controlled room, under a 12-hour dark/12-hour light cycle. Pelleted food (3437PXL15 and CARGILL) and water were provided ad-libitum.

Twenty one GCaMP6f mice [*C57BL/6J-Tg(Thy1-GCaMP6f) GP5.17Dkim/J*, the Jackson Laboratory, USA] were used for this study (13 female and 8 male). The mouse head was immobilized using a custom stereotactic frame (Narishige International Limited, London, UK). Blood oxygen saturation, heart rate, and mouse body temperature were continuously monitored (PhysioSuite, Kent Scientific, Torrington, CT, USA), and the body temperature was kept within physiological range with a heating pad. The hair on the mouse head was first trimmed and then removed using shaving cream to ensure optimal ultrasound coupling. Seven mice were imaged after scalp removal because of skin pigmentation. The mice were subcutaneously injected with buprenorphine (0.1 mg/kg) 30 min before scalp removal. A 40% dilution of phosphate-buffered saline in ultrasound gel (Aquasonic Clear, Parker Laboratories Inc., Fairfield, NJ, USA) was deposited on mouse's scalp and brought into contact with the transparent membrane of the water tank to ensure unobstructed delivery of light and ultrasound into the mouse brain.

Two mice (6.5 weeks old) were anesthetized using ketamine-xylazine cocktail (100 and 5 mg/kg, respectively) and sonicated through an intact scalp and skull with 150-ms duration pulses at 3 MHz delivered sequentially every 11 s onto two different locations in the mouse cortex separated by 1 mm. Epifluorescence calcium recordings were corrected with a moving baseline (0 to 0.05 Hz) to remove signal drifts because of laser energy fluctuations and photobleaching. To reduce the spatial noise, a Gaussian filter with a SD of 0.5 pixels (~20 µm) was applied to the image stack.

Other 19 mice (6 to 8 weeks old) were sonicated using the sequences shown in Table 1 under isoflurane anesthesia [3% (v/v) for induction and 1.2% (v/v) for maintenance]. For CSD imaging, the acquired image stacks were band-pass–filtered between 0 and 8 Hz and a Gaussian spatial filter with a SD of 1 pixel (~40 μm) was used to reduce noise. Last, the skull of a 9-week-old male mouse was used to measure its insertion loss and ultrasound-focusing properties upon transcranial transmission.

### RSC for single FUS emissions

To increase the SNR of fluorescence responses to single FUS emissions, we take advantage of the high interhemisphere correlation that is present in the wide-field calcium recordings. For this, a simple subtraction of the mirror image on the hemisphere opposite to the FUS delivery efficiently cancels the resting state oscillations, thus increasing SNR by 5 dB on average (Fig. 2C). Using a spatial Gaussian filter of 2 pixels (80 μm) further increased the SNR by up to 12 dB on average. When applied to averaged traces from multiple sonications, the SNR improvement is reduced to 2.5 dB, making the RSC method suitable for improving sensitivity for detecting responses to single sonications.

### In vitro characterization of FUS emission on GFP-expressing *Escherichia coli* colonies

*Escherichia coli* DG1 were transformed with pNCS_GFP_his6, a construct based on the bacterial expression vector pNCS that triggers constitutive expression of the transgene when bacterial cells reach high density (*41*). The GFP derivative used was the cycle 3 mutant published by Stemmer and colleagues (*42*). Chemical transformation was carried out according to the protocol of Okayama and colleagues (*43*).

Bacteria were expanded for 1 hour in shaken liquid culture at 37°C in the absence of selection antibiotic before streaking 100 μl onto 10-cm Agar LB plates containing ampicillin (100 μg/ml). Fluorescence measurements were performed following overnight growth at 36°C and were kept in agar at room temperature (23°C) during the experiments.

The recorded image stack is first low-pass–filtered in frequency domain from 0 to 8 Hz and referenced to a moving baseline (0 to 0.1 Hz) to correct for laser fluctuations and bleaching of the GFP protein. Two-dimensional Gaussian blurring with a SD of 1.5 pixels (~60 μm) is applied to every frame to reduce spatial noise.

FUS at 3 MHz frequency was delivered for 150 ms to reproduce the conditions of the in vivo experiments. The emission was repeated for five cycles with a period of 2 s.

### In vitro characterization of fluorescence dependence on temperature

A male GCaMP6f mouse (9 weeks old) was euthanized by ketamin/xylazine overdose, and coronal brain slices (1 mm thick) were extracted and placed in artificial cerebrospinal fluid on top of a heating plate and inside a water bath. The heating plate was linked to a thermometer to operate in a retro-control loop. Fluorescence was monitored at the lowest laser power level possible to mitigate photobleaching. Temperature was monitored using a thermocouple tip (IT-23, Physitemp Instruments, Clifton, NJ, USA) placed as close as possible to the brain slice and acquired using an NI 9213 USB interface (National Instruments, Austin, TX, USA). The brain slice is first heated with the plate for 5 min and then cooled down with ice in the water bath for another 5 min. For each acquisition, all images were registered to the first frame to compensate for potential motion artifacts. A mean fluorescent value was extracted for each time point and manually aligned in time with the temperature curve measured with thermocouple. Localized outliers in the fluorescence curves were also excluded whenever clearly corresponding to an ice pouring event.

### Thermal modeling

The thermal response was calculated using the bioheat model (*29*) described by the Pennes equation (*44*), i.e.

$$\rho C\frac{\partial T}{\partial t} = \kappa\nabla^2 T + q + w\rho_b C_b(T - T_a) \quad (2)$$

where $T$ is the temperature, $\rho$ = 1027 (kg/m$^3$) is the mass density, $C$ = 3640 (J kg$^{-1}$°C$^{-1}$) is specific heat capacity, and $\kappa$ = 0.51 (W m$^{-1}$ °C$^{-1}$) is thermal conductivity (*27*). $q$ (W/m$^3$) corresponds to the rate of heat production, $w$ (s$^{-1}$) is the blood perfusion rate, $\rho_b$ (kg/m$^3$) is the blood density, $C_b$ (J kg$^{-1}$ °C$^{-1}$) is the blood specific heat, and $T_a$ is the ambient blood temperature. Owing to the fast thermal dynamics induced by the FUS delivery, the third term on the right-hand side of Eq. 2 did not affect the simulation outcome. We first simulated the ultrasound focus using a linear model (*25*). The ultrasound intensity was then calculated and used in conjunction with an average ultrasound attenuation of 16 Np/m to calculate $q$. The equation was solved using axially symmetric boundary conditions. Because of the scalability of the obtained solution, no insight could be gained by altering the ultrasound intensity or the absorption.

### Functional connectivity analysis

The wide-field fluorescence data of six mice (scalp removed) were rotated, cropped, and coregistered to a mouse brain atlas. After calculating the relative change in fluorescence, the data were band-pass–filtered in frequency domain (0.1 to 1 Hz) following (*30*) and the first and last 50 frames cropped to eliminate filtering artifacts. A total of seven brain areas for each hemisphere were chosen to perform the analysis. The average of a square of 7 × 7 pixels was used as seed to calculate the Pearson correlation coefficient to every pixel inside the brain. To generate the connectivity matrix, the correlation coefficient was averaged inside 13 other brain areas for each seed. To perform a paired $t$ test with the calcium data acquired before and after the sonication, we first $z$-transformed the correlation to standardize its distribution. Then, the $P$ value was used to mask the difference between the averaged connectivity matrices (after sonication minus before sonication). To control for false discovery rate in multiple testing (Fig. 4H), the $P$ value was corrected using a method described elsewhere (*45*).

### Histological analysis

Brains were rapidly extracted after decapitation of the animals under 5% isoflurane anesthesia and put into 4% paraformaldehyde in 0.15 M phosphate buffer for 24 hours at 4°C. Brains were cryoprotected in 30% sucrose in phosphate-buffered saline for 72 hours and then cut at a microtome into 20- to 30-μm-thick coronal sections.

Sections from mice sonicated with sequence 1 (see Table 1) and euthanized 24 hours after sonication were mounted onto glass slides, dried at 55°C for 5 min, and then subjected to TUNEL assay to detect DNA breaks formed during the final phase of apoptosis. A commercially

available TUNEL assay kit was used (Promega, no. G3250), following the instructions from the kit. Deoxyribonuclease (DNAse)–treated slices (ribonuclease-free DNAse; QIAGEN, no. 79254) from untreated animals were used as positive control (fig. S2). Slices were coverslipped using FluroShield with DAPI (Sigma-Aldrich, F6057). Other sections from mice sonicated with sequence 1 were subjected to Fluoro-Jade C (Fluoro-Jade C, Biosensis) staining to detect apoptotic neurons, following the protocol described in (*46*). Mice sonicated with other sequences were euthanized immediately after the end of the experiment.

To increase the likelihood of finding the sonicated brain region in the absence of a clear lesion with sequence 1, ultrasound was delivered in nine sonication spots separated by 500 μm following a sagittal line parallel to the midline 1 mm into the right hemisphere (Fig. 4G) in three mice.

For c-Fos (c-Fos antibody, rabbit Santa Cruz Biotechnology, Sc 7202 AB_2106765; diluted 1:500), CD68 (CD68 antibody, rat monoclonal, AbD Serotec MCA1057; diluted 1:1000), and the podocalyxin/glial fibrillary acidic protein (GFAP) immunohistochemistry staining (podocalyxin antibody, goat, R&D Systems, AF1556; diluted 1:500; and GFAP antibody, rabbit, DAKO, Z0334; diluted 1:1000), sections were incubated overnight at 4°C with the first antibodies in tris-NaCl buffer containing 4% normal donkey serum and 2% Triton X-100. After intensive rinsing, they were incubated with secondary antibodies conjugated to Cy3, Cy5, or Alexa 488 (Jackson ImmunoResearch; all 1:500) in tris buffer containing 4% normal donkey serum for 45 min at room temperature. Sections were washed in tris-NaCl, mounted, and coverslipped using FluroShield with DAPI (Sigma-Aldrich F6057).

High-magnification images of immunofluorescence staining were acquired by laser scanning confocal microscopy (Zeiss LSM 700). Stacks of 4 to 11 confocal layers (512 × 512 pixels) spaced by 1 μm were recorded using a 25× lens with the pinhole set to 1.0 Airy units. Larger images were recorded on the Zeiss Apotome 1 using a nonimmersing 20× objective and the software blue Zen (Zeiss) for tiling.

## SUPPLEMENTARY MATERIALS

Supplementary material for this article is available at https://science.org/doi/10.1126/sciadv.abi5464

View/request a protocol for this paper from *Bio-protocol*.

## REFERENCES AND NOTES


1. Y. Meng, K. Hynynen, N. Lipsman, Applications of focused ultrasound in the brain: From thermoablation to drug delivery. *Nat. Rev. Neurol.* **17**, 7–22 (2021).
2. B. Larrat, M. Pernot, J. F. Aubry, E. Dervishi, R. Sinkus, D. Seilhean, Y. Marie, A. L. Boch, M. Fink, M. Tanter, MR-guided transcranial brain HIFU in small animal models. *Phys. Med. Biol.* **55**, 365–388 (2010).
3. V. Ozenne, C. Constans, P. Bour, M. D. Santin, R. Valabrègue, H. Ahnine, P. Pouget, S. Lehéricy, J. Aubry, B. Quesson, MRI monitoring of temperature and displacement for transcranial focus ultrasound applications. *Neuroimage* **204**, 116236 (2019).
4. O. Naor, S. Krupa, S. Shoham, Ultrasonic neuromodulation. *J. Neural Eng.* **13**, 031003 (2016).
5. N. Lipsman, Y. Meng, A. J. Bethune, Y. Huang, B. Lam, M. Masellis, N. Herrmann, C. Heyn, I. Aubert, A. Boutet, G. S. Smith, K. Hynynen, S. E. Black, Blood-brain barrier opening in Alzheimer's disease using MR-guided focused ultrasound. *Nat. Commun.* **9**, 2336 (2018).
6. S. Wang, T. Kugelman, A. Buch, M. Herman, Y. Han, M. E. Karakatsani, S. A. Hussaini, K. Duff, E. E. Konofagou, Non-invasive, focused ultrasound-facilitated gene delivery for optogenetics. *Sci. Rep.* **7**, 39955 (2017).
7. M. D. Menz, P. Ye, K. Firouzi, A. Nikoozadeh, K. B. Pauly, P. Khuri-Yakub, S. A. Baccus, Radiation force as a physical mechanism for ultrasonic neurostimulation of the ex vivo retina. *J. Neurosci.* **39**, 6251–6264 (2019).
8. Y. Jiang, H. J. Lee, L. Lan, H.-a. Tseng, C. Yang, H.-Y. Man, X. Han, J.-X. Cheng, Optoacoustic brain stimulation at submillimeter spatial precision. *Nat. Commun.* **11**, 881 (2020).
9. M. Mohammadjavadi, P. P. Ye, A. Xia, J. Brown, G. Popelka, K. B. Pauly, Elimination of peripheral auditory pathway activation does not affect motor responses from ultrasound neuromodulation. *Brain Stimul.* **12**, 901–910 (2019).
10. Y. Yuan, Z. Wang, M. Liu, S. Shoham, Cortical hemodynamic responses induced by low-intensity transcranial ultrasound stimulation of mouse cortex. *Neuroimage* **211**, 116597 (2020).
11. E. Kim, E. Anguluan, J. G. Kim, Monitoring cerebral hemodynamic change during transcranial ultrasound stimulation using optical intrinsic signal imaging. *Sci. Rep.* **7**, 13148 (2017).
12. J. A. N. Fisher, I. Gumenchuk, Low-intensity focused ultrasound alters the latency and spatial patterns of sensory-evoked cortical responses in vivo. *J. Neural Eng.* **15**, 035004 (2018).
13. T. Sato, M. G. Shapiro, D. Y. Tsao, Ultrasonic neuromodulation causes widespread cortical activation via an indirect auditory mechanism. *Neuron* **98**, 1031–1041.e5 (2018).
14. W. Lee, H.-C. Kim, Y. Jung, Y. A. Chung, I.-U. Song, J.-H. Lee, S.-S. Yoo, Transcranial focused ultrasound stimulation of human primary visual cortex. *Sci. Rep.* **6**, 34026 (2016).
15. Y. Younan, T. Deffieux, B. Larrat, M. Fink, M. Tanter, J.-F. Aubry, Influence of the pressure field distribution in transcranial ultrasonic neurostimulation. *Med. Phys.* **40**, 082902 (2013).
16. G. Li, W. Qiu, J. Hong, Q. Jiang, M. Su, P. Mu, G. Yang, Y. Li, C. Wang, H. Zhang, H. Zheng, Imaging-guided dual-target neuromodulation of the mouse brain using array ultrasound. *IEEE Trans. Ultrason. Ferroelectr. Freq. Control* **65**, 1583–1589 (2018).
17. C. Grienberger, A. Konnerth, Imaging calcium in neurons. *Neuron* **73**, 862–885 (2012).
18. T.-W. Chen, T. J. Wardill, Y. Sun, S. R. Pulver, S. L. Renninger, A. Baohan, E. R. Schreiter, R. A. Kerr, M. B. Orger, V. Jayaraman, L. L. Looger, K. Svoboda, D. S. Kim, Ultrasensitive fluorescent proteins for imaging neuronal activity. *Nature* **499**, 295–300 (2013).
19. H. Mestre, T. Du, A. M. Sweeney, G. Liu, A. J. Samson, W. Peng, K. N. Mortensen, F. F. Staeger, P. A. R. Bork, L. Bashford, E. R. Toro, J. Tithof, D. H. Kelley, J. H. Thomas, P. G. Hjorth, E. A. Martens, R. I. Mehta, O. Solis, P. Blinder, D. Kleinfeld, H. Hirase, Y. Mori, M. Nedergaard, Cerebrospinal fluid influx drives acute ischemic tissue swelling. *Science* **367**, (2020).
20. A. Louveau, J. Herz, M. N. Alme, A. F. Salvador, M. Q. Dong, K. E. Viar, S. G. Herod, J. Knopp, J. C. Setliff, A. L. Lupi, S. Da Mesquita, E. L. Frost, A. Gaultier, T. H. Harris, R. Cao, S. Hu, J. R. Lukens, I. Smirnov, C. C. Overall, G. Oliver, J. Kipnis, CNS lymphatic drainage and neuroinflammation are regulated by meningeal lymphatic vasculature. *Nat. Neurosci.* **21**, 1380–1391 (2018).
21. G. Katona, G. Szalay, P. Maák, A. Kaszás, M. Veress, D. Hillier, B. Chiovini, E. S. Vizi, B. Roska, B. Rózsa, Fast two-photon in vivo imaging with three-dimensional random-access scanning in large tissue volumes. *Nat. Methods* **9**, 201–208 (2012).
22. J. Fan, J. Suo, J. Wu, H. Xie, Y. Shen, F. Chen, G. Wang, L. Cao, G. Jin, Q. He, T. Li, G. Luan, L. Kong, Z. Zheng, Q. Dai, Video-rate imaging of biological dynamics at centimetre scale and micrometre resolution. *Nat. Photonics* **13**, 809–816 (2019).
23. Y. Kamei, M. Suzuki, K. Watanabe, K. Fujimori, T. Kawasaki, T. Deguchi, Y. Yoneda, T. Todo, S. Takagi, T. Funatsu, S. Yuba, Infrared laser-mediated gene induction in targeted single cells in vivo. *Nat. Methods* **6**, 79–81 (2009).
24. Z. Chen, X. L. Deán-Ben, S. Gottschalk, D. Razansky, Hybrid system for in vivo epifluorescence and 4D optoacoustic imaging. *Opt. Lett.* **42**, 4577–4580 (2017).
25. H. Estrada, A. Özbek, J. Robin, S. Shoham, D. Razansky, Spherical array system for high-precision transcranial ultrasound stimulation and optoacoustic imaging in rodents. *IEEE_J_UFFC* **68**, 107–115 (2021).
26. W. D. O'Brien Jr., Ultrasound-biophysics mechanisms. *Prog. Biophys. Mol. Biol.* **93**, 212–255 (2007).
27. C. M. Collins, M. B. Smith, R. Turner, Model of local temperature changes in brain upon functional activation. *J. Appl. Physiol.* **97**, 2051–2055 (2004).
28. S. A. Goss, L. A. Frizzell, F. Dunn, Ultrasonic absorption and attenuation in mammalian tissues. *Ultrasound Med. Biol.* **5**, 181–186 (1979).
29. J. Soneson, High intensity focused ultrasound simulator. (2020).
30. J. V. Cramer, B. Gesierich, S. Roth, M. Dichgans, M. Düring, A. Liesz, In vivo widefield calcium imaging of the mouse cortex for analysis of network connectivity in health and brain disease. *Neuroimage* **199**, 570–584 (2019).
31. E. S. Lein, M. J. Hawrylycz, N. Ao, M. Ayres, A. Bensinger, A. Bernard, A. F. Boe, M. S. Boguski, K. S. Brockway, E. J. Byrnes, L. Chen, L. Chen, T. M. Chen, M. Chi Chin, J. Chong, B. E. Crook, A. Czaplinska, C. N. Dang, S. Datta, N. R. Dee, A. L. Desaki, T. Desta, E. Diep, T. A. Dolbeare, M. J. Donelan, H. W. Dong, J. G. Dougherty, B. J. Duncan, A. J. Ebbert, G. Eichele, L. K. Estin, C. Faber, B. A. Facer, R. Fields, S. R. Fischer, T. P. Fliss, C. Frensley, S. N. Gates, K. J. Glattfelder, K. R. Halverson, M. R. Hart, J. G. Hohmann, M. P. Howell, D. P. Jeung, R. A. Johnson, P. T. Karr, R. Kawal, J. M. Kidney, R. H. Knapik, C. L. Kuan, J. H. Lake, A. R. Laramee, K. D. Larsen, C. Lau, T. A. Lemon, A. J. Liang, Y. Liu, L. T. Luong, J. Michaels, J. J. Morgan, R. J. Morgan, M. T. Mortrud, N. F. Mosqueda, L. L. Ng, R. Ng, G. J. Orta, C. C. Overly, T. H. Pak, S. E. Parry, S. D. Pathak, O. C. Pearson,

R. B. Puchalski, Z. L. Riley, H. R. Rockett, S. A. Rowland, J. J. Royall, M. J. Ruiz, N. R. Sarno, K. Schaffnit, N. V. Shapovalova, T. Sivisay, C. R. Slaughterbeck, S. C. Smith, K. A. Smith, B. I. Smith, A. J. Sodt, N. N. Stewart, K. R. Stumpf, S. M. Sunkin, M. Sutram, A. Tam, C. D. Teemer, C. Thaller, C. L. Thompson, L. R. Varnam, A. Visel, R. M. Whitlock, P. E. Wohnoutka, C. K. Wolkey, V. Y. Wong, M. Wood, M. B. Yaylaoglu, R. C. Young, B. L. Youngstrom, X. Feng Yuan, B. Zhang, T. A. Zwingman, A. R. Jones, Genome-wide atlas of gene expression in the adult mouse brain. *Nature* **445**, 168–176 (2007).

32. J. A. Hartings, C. W. Shuttleworth, S. A. Kirov, C. Ayata, J. M. Hinzman, B. Foreman, R. D. Andrew, M. G. Boutelle, K. Brennan, A. P. Carlson, M. A. Dahlem, C. Drenckhahn, C. Dohmen, M. Fabricius, E. Farkas, D. Feuerstein, R. Graf, R. Helbok, M. Lauritzen, S. Major, A. I. Oliveira-Ferreira, F. Richter, E. S. Rosenthal, O. W. Sakowitz, R. Sánchez-Porras, E. Santos, M. Schöll, A. J. Strong, A. Urbach, M. B. Westover, M. K. Winkler, O. W. Witte, J. Woitzik, J. P. Dreier, The continuum of spreading depolarizations in acute cortical lesion development: Examining Leão's legacy. *J. Cereb. Blood Flow Metab.* **37**, 1571–1594 (2017).
33. J. R. Lakowicz, in *Principles of Fluorescence Spectroscopy* (Springer US, 1983), pp. 257–301.
34. M. Nedergaard, A. J. Hansen, Spreading depression is not associated with neuronal injury in the normal brain. *Brain Res.* **449**, 395–398 (1988).
35. T. Houben, I. C. Loonen, S. M. Baca, M. Schenke, J. H. Meijer, M. D. Ferrari, G. M. Terwindt, R. A. Voskuyl, A. Charles, A. M. van den Maagdenberg, E. A. Tolner, Optogenetic induction of cortical spreading depression in anesthetized and freely behaving mice. *J. Cereb. Blood Flow Metab.* **37**, 1641–1655 (2017).
36. C. Ayata, M. Shimizu-Sasamata, E. H. Lo, J. L. Noebels, M. A. Moskowitz, Impaired neurotransmitter release and elevated threshold for cortical spreading depression in mice with mutations in the $\alpha$1A subunit of P/Q type calcium channels. *Neuroscience* **95**, 639–645 (1999).
37. M. Ueda, J. Bure, J. Fischer, Spreading depression elicited by thermal effects of ultrasonic irradiation of cerebral cortex in rats. *J. Neurobiol.* **8**, 381–393 (1977).
38. K. Suhling, L. M. Hirvonen, J. A. Levitt, P.-H. Chung, C. Tregidgo, A. Le Marois, D. A. Rusakov, K. Zheng, S. Ameer-Beg, S. Poland, S. Coelho, R. Henderson, N. Krstajic, Fluorescence lifetime imaging (FLIM): Basic concepts and some recent developments. *Med. Photonics* **27**, 3–40 (2015).
39. M. Chamanzar, M. G. Scopelliti, J. Bloch, N. Do, M. Huh, D. Seo, J. Iafrati, V. S. Sohal, M.-R. Alam, M. M. Maharbiz, Ultrasonic sculpting of virtual optical waveguides in tissue. *Nat. Commun.* **10**, 92 (2019).
40. R. Beisteiner, E. Matt, C. Fan, H. Baldysiak, M. Schönfeld, T. Philippi Novak, A. Amini, T. Aslan, R. Reinecke, J. Lehrner, A. Weber, U. Reime, C. Goldenstedt, E. Marlinghaus, M. Hallett, H. Lohse-Busch, Transcranial pulse stimulation with ultrasound in Alzheimer's disease – A new navigated focal brain therapy. *Adv. Sci.* **7**, 1902583 (2020).
41. N. C. Shaner, G. G. Lambert, A. Chammas, Y. Ni, P. J. Cranfill, M. A. Baird, B. R. Sell, J. R. Allen, R. N. Day, M. Israelsson, M. W. Davidson, J. Wang, A bright monomeric green fluorescent protein derived from Branchiostoma lanceolatum. *Nat. Methods* **10**, 407–409 (2013).
42. A. Crameri, E. A. Whitehorn, E. Tate, W. P. C. Stemmer, Improved green fluorescent protein by molecular evolution using dna shuffling. *Nat. Biotechnol.* **14**, 315–319 (1996).
43. H. Inoue, H. Nojima, H. Okayama, High efficiency transformation of Escherichia coli with plasmids. *Gene* **96**, 23–28 (1990).
44. H. H. Pennes, Analysis of tissue and arterial blood temperatures in the resting human forearm. *J. Appl. Physiol.* **1**, 93–122 (1948).
45. Y. Benjamini, Y. Hochberg, Controlling the false discovery rate: A practical and powerful approach to multiple testing. *J. R. Stat. Soc. B. Methodol.* **57**, 289–300 (1995).
46. A. Ehara, S. Ueda, Application of Fluoro-Jade C in acute and chronic neurodegeneration models: Utilities and staining differences. *ACTA Histochem. Cytochem.* **42**, 171–179 (2009).

**Acknowledgments:** We thank M. Rudin and A. Schröter for helpful discussions. We also acknowledge the valuable help of M. Reiss with the mouse experiments and of S. Pérez-López and U. Hoffman in the ultrasound attenuation experiments. **Funding:** This work is supported by the National Institutes of Health grant UF1-NS107680 (to S.S. and D.R.), European Research Council grant ERC-2015-CoG-682379 (to D.R.), National Institutes of Health grant 5R01NS109885-02 (to S.S.), and ETH Zurich Postdoctoral Fellowship (to J.R.) **Author contributions:** D.R. and S.S. conceived the experimental system. H.E., A.Ö., and Z.C. developed the experimental system. H.E. and J.R. carried out the experiments in mice with the help of A.Ö., Z.C., and Q.Z. H.E. developed the software and performed data analysis and visualization. J.R. preprocessed the data. B.I.R. and M.A. provided bacterial colonies. A.M., D.B., and M.A. designed and performed the histology analysis, staining, and imaging. D.R. and S.S. supervised the study. H.E. and J.R. wrote the manuscript. All authors reviewed and edited the manuscript. **Competing interests:** The authors declare that they have no competing interests. **Data and materials availability:** All data needed to evaluate the conclusions in the paper are present in the paper and/or the Supplementary Materials.

Submitted 16 March 2021
Accepted 19 October 2021
Published 8 December 2021
10.1126/sciadv.abi5464